
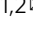





## Spin dynamics, loop formation and cooperative reversal in artificial quasicrystals with tailored exchange coupling

Vinayak Shantaram Bhat <sup>1,2</sup>, Sho Watanabe<sup>1</sup>, Florian Kronast <sup>3</sup>, Korbinian Baumgaertl<sup>1</sup> & Dirk Grundler <sup>1,4</sup>

Aperiodicity and un-conventional rotational symmetries allow quasicrystalline structures to exhibit unusual physical and functional properties. In magnetism, artificial ferromagnetic quasicrystals exhibited knee anomalies suggesting reprogrammable magnetic properties via non-stochastic switching. However, the decisive roles of short-range exchange and long-range dipolar interactions have not yet been clarified for optimized reconfigurable functionality. We report broadband spin-wave spectroscopy and X-ray photoemission electron microscopy on different quasicrystal lattices consisting of ferromagnetic  $\text{Ni}_{81}\text{Fe}_{19}$  nanobars arranged on aperiodic Penrose and Ammann tilings with different exchange and dipolar interactions. We imaged the magnetic states of partially reversed quasicrystals and analyzed their configurations in terms of the charge model, geometrical frustration and the formation of flux-closure loops. Only the exchange-coupled lattices are found to show aperiodicity-specific collective phenomena and non-stochastic switching. Both, exchange and dipolarly coupled quasicrystals show magnonic excitations with narrow linewidths in minor loop measurements. Thereby reconfigurable functionalities in spintronics and magnonics become realistic.

<sup>1</sup>Laboratory of Nanoscale Magnetic Materials and Magnonics, Institute of Materials (IMX), École Polytechnique Fédérale de Lausanne (EPFL), 1015 Lausanne, Switzerland. <sup>2</sup>International Research Centre MagTop, Institute of Physics, Polish Academy of Sciences, 02668 Warsaw, Poland. <sup>3</sup>Helmholtz-Zentrum Berlin für Materialien und Energie GmbH, Hahn-Meitner-Platz 1, D-14109 Berlin, Germany. <sup>4</sup>Institute of Electrical and Micro Engineering (IEM), École Polytechnique Fédérale de Lausanne (EPFL), 1015 Lausanne, Switzerland. ✉email: [vbat@magtop.ifpan.edu.pl](mailto:vbat@magtop.ifpan.edu.pl); [dirk.grundler@epfl.ch](mailto:dirk.grundler@epfl.ch)

Quasicrystals exhibit aperiodic long-range order and unconventional rotational symmetry, but no translational invariance. Since their discovery<sup>1,2</sup> the impact of aperiodicity on fundamental physical phenomena is pursued with great interest<sup>2</sup>. One powerful avenue to gain insight resides in the materials-by-design approach making use of nanofabrication and imaging techniques<sup>3</sup>. Thereby microscopic understanding of, e.g., geometrical frustration in spin ice systems was achieved. The artificial spin ices (ASIs) consisted of either disconnected or interconnected ferromagnetic nanobars that were arranged on strictly periodic lattices with translational invariance<sup>4–6</sup>. In both types of ASIs cooperative phenomena were found and analyzed via spin ice rules, charge model and energy minimization through clockwise (CW) and counter-clockwise (CCW) flux-closure loops (FCLs)<sup>7,8</sup>. Vortex-like microstates, i.e., flux-closure loops in a lattice (which are sometimes called microvortices), indicated energy minimization due to magnetic coupling<sup>9</sup>. Tailored dipolar interaction was named key for devices<sup>10</sup> based on e.g., reproducible microstates upon cycling an applied magnetic field<sup>11,12</sup>. The spin dynamics in periodic ASIs with reconfigurable magnetic configurations and intentionally introduced magnetic defects have already generated enormous interest<sup>12–18</sup>. Still Iacocca et al. pointed out very recently that dipolar coupling in real ASI might not be sufficient for reconfigurable magnon waveguides<sup>19</sup> consistent with earlier experiments<sup>20</sup>. For artificial magnetic quasicrystals (AMQs) unconventional magnetic properties and non-stochastic switching were reported for both interconnected lattices with exchange coupling and lattices with edge-to-edge separations of up to about 150 nm between nanomagnets exhibiting dipolar interaction only<sup>3,21–24</sup>.

Following the orthodox understanding<sup>25</sup> and recently performed micromagnetic simulations one anticipates aperiodicity-induced phenomena for edge-to-edge separations even wider than 150 nm<sup>24</sup>. Particularly, aperiodic quasicrystals promise a plethora of reconfigurable magnetic configurations due to non-stochastic switching in a global magnetic field, while periodic lattices would require the serial writing process based on a magnetic force microscope<sup>25</sup>. Domains and domain walls between differently oriented lattice segments of ASIs have been foreseen already as conduits which steer magnons in a reconfigurable manner inside the magnetic lattice<sup>26</sup> or in an underlayer<sup>19</sup>. However, the following questions are unanswered: (1) How do the cooperative phenomena show up in real samples when one systematically varies the type and relative strength of coupling among aperiodic nanobars? (2) What is the origin of the knee-like anomalies which were reported for the magnetic hysteresis of quasicrystalline Penrose P2 tilings?<sup>3</sup> (3) How do functional properties of ferromagnetic Penrose P2 and P3 tilings compare? They belong to the same class of ten-fold rotationally symmetric quasicrystal lattices but consist of different geometric prototiles<sup>27</sup>. In this article, we report on dynamic and quasi-static investigations based on broadband spin-wave spectroscopy (Fig. 1a) and magnetic imaging (Fig. 1), respectively, performed on ten-fold rotationally symmetric Penrose P2, P3 and the eight-fold rotationally symmetric Ammann tilings. We address the open questions by magnetic resonance spectra taken in the major loop and the hysteretic regime as well as X-ray photoemission electron microscopy (XPEEM) using X-ray magnetic circular dichroism (XMCD) with high spatial resolution (“Methods”).

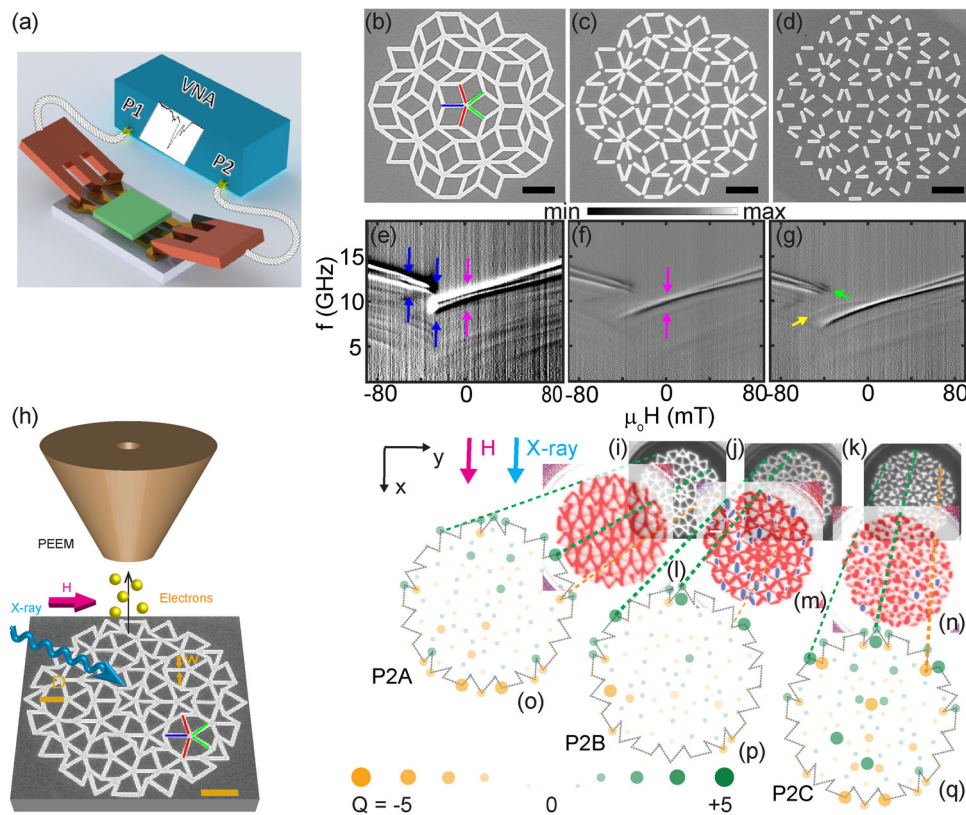
For our studies we prepared artificial magnetic quasicrystals in the form of nanobars (Fig. 1) out of the magnetically isotropic alloy Ni<sub>81</sub>Fe<sub>19</sub> (Py) on Penrose P3 (Fig. 1b–d), P2 (Fig. 1h–q), and Ammann (Fig. 2a–c) quasicrystal lattices using nanofabrication techniques. The width  $w$  of nanobars, their thickness and inter-vertex spacing were kept at 120, 25, and 810 nm, respectively. We varied the lengths  $D$  of nanobars from sample to sample between

810 and 408 nm. Thereby we created quasicrystals which consisted of interconnected (A), partially connected (B) and fully separated nanobars (C), respectively (compare Fig. 1b–d). The interconnected nanobars joining in the vertices of an AMQ of kind A were both exchange and dipolarly coupled. Separated nanobars in kind B and C were dipolarly coupled only. In sample B (sample C) opposing nanobars exhibited edge-to-edge separations of up to about 200 nm (400 nm). The imaging presented here show that for non-stochastic switching and cooperative reversal in Penrose and Ammann tilings the recently explored dipolar coupling<sup>24</sup> is not sufficient. We observe significant domain formation only when quasicrystalline Penrose P3 and Ammann tilings are exchange-coupled. Both exchange- and dipolarly coupled lattices show reprogrammable magnonic excitations of narrow linewidth. Our findings are key when designing quasicrystals for field-controlled functionalities exploiting return-point memory and reproducible magnetic states<sup>11,26,28</sup>.

## Results and discussion

**Broadband spin-wave spectroscopy in the major loop.** For the presentation of the results we decompose the Penrose lattices reported in Fig. 1 into three types of nanobars, i.e., Type I, Type II, and Type III based on the angle  $\phi$  that the nanobars take with respect to the direction of magnetic field  $H$  used in Fig. 1: Type I exhibits  $\phi = 0^\circ$ , Type II  $\phi = \pm 36^\circ$ , and Type III  $\phi = \pm 72^\circ$ . Considering ref. <sup>29</sup> we calculated shape anisotropy fields  $\mu_0 H_{\text{ani}}$  for individual nanobars of lengths 810, 609, and 408 nm and obtained 147, 140, and 117 mT, respectively. Note that the maximum field  $\mu_0 |H_{\text{max}}| = 90$  mT that was available in the broadband spin-wave spectroscopy setup was smaller than the calculated fields  $\mu_0 H_{\text{ani}}$ . As a consequence, nanobars perpendicular to the applied field could not be saturated. The magnetization reversal in a nanobar can occur via coherent, curling or buckling mode. The curling mode of magnetization reversal, as opposed to coherent rotation, avoids the creation of stray magnetic field by going through a vortex state; thereby, magnetization lies parallel to the surface<sup>30</sup>. The estimated nucleation field for incoherent reversal in an ideal isolated nanobar with  $D = 810$  nm via curling amounted to 70 mT<sup>31</sup>. The minimum reversal field for coherent rotation was about the same value. Considering these values, we expected the field regime ranging from  $+90$  mT  $\leq \mu_0 H \leq -90$  mT to be large enough to reverse the magnetization of Type I and II nanobars but not of individual nanobars of Type III exhibiting an angle  $|\phi|$  of  $72^\circ$ .

In the following we present and discuss broadband spectroscopy data obtained on P3 lattices and Ammann tilings for which we have observed large domain formation in the XPEEM imaging experiments. We collect the scattering parameters  $S$  from the vector network analyzer as a function of frequency  $f$  at the constant applied magnetic field,  $\mu_0 H$ , and angle  $\phi$ , and this corresponds to a single spin-wave spectrum at one  $\mu_0 H$  and  $\phi$  value. We then subtract spin-wave spectra taken at successive fields  $\mu_0 H$ ; that is, we obtain  $\Delta S(i) = S[H(i+1), \phi] - S[H(i), \phi]$ . In Fig. 1e–g, we display spectra taken on Penrose P3 tilings when varying  $\mu_0 H$  from  $+90$  mT to  $-90$  mT. The black and white contrast lines against the gray background represent different spin-wave branches. For all three samples we see two strong branches at large absolute field values consistent with the interconnected AMQs reported earlier in ref. <sup>32</sup>. We attribute the branches to resonances in Type I (highest frequency) and Type II (second highest frequency) nanobars. Considering a field of 90 mT, the branch frequencies decrease from (e) to (g), i.e., for the interconnected nanobars (P3A) the two prominent branches reside at overall larger frequencies than for the disconnected nanobars (P3C).



**Fig. 1** Broadband spin-wave spectroscopy and X-ray photoemission electron microscopy (XPEEM) study of artificial magnetic quasicrystals (AMQs).

**a** Sketch of broadband spin-wave spectroscopy showing the two ports, P1 and P2, of a vector network analyzer (VNA) connected to a coplanar waveguide via microwave probes. Scanning electron microscopy (SEM) images showing 3rd generation Penrose P3 lattices: **b** P3A for which nanobars are fully connected, **c** P3B with partially connected nanobars, and **d** P3C with disconnected nanobars. The scale bars correspond to 1  $\mu\text{m}$ . The Type I, Type II, and Type III nanobars are indicated by blue, green and red colored lines, respectively, in **(b)**. The scale bars correspond to 1  $\mu\text{m}$ . Gray-scale spin-wave spectra obtained on 8th generation **(e)** P3A, **(f)** P3B, and **(g)** P3C samples. The magnetic field was applied along the horizontal direction of graphs **(b)**–**(d)** and varied from +90 mT to –90 mT in a step-wise manner. In the field regime between the blue arrows **(e)** the reversal of the AMQ takes place. The magenta color arrows mark  $H = 0$  in **(e)**. The green arrow in **(g)** marks the high-frequency mode in the reversal regime. The yellow arrow highlights the branch attributed to nanomagnets being almost perpendicular to the applied field. **h** Sketch of the XPEEM imaging experiment performed on ferromagnetic quasicrystals. Here a Penrose P2 tiling is shown as an SEM image.  $D$  and  $w$  represent the length and width of a nanobar, respectively. XPEEM topography images of nanobars arranged on Penrose P2 lattices **(i)** P2A, **(j)** P2B, and **(k)** P2C. XPEEM X-ray magnetic circular dichroism (XMCD) images taken on **(l)** P2A, **(m)** P2B, and **(n)** P2C. Analysis of the magnetic configurations of vertices based on the charge ( $Q$ ) model for **(o)** P2A, **(p)** P2B, and **(q)** P2C. The magnitude of  $Q$  is given by diameter and intensity of circles (legend). Orange (green) color indicates negative (positive) charge. The broken lines guide the eye for the allocation of charges to a specific vertex. For the configurations shown the maximum evaluated  $|Q|$  amounted to 3. The XPEEM images were taken at  $\mu_0 H = 0$  mT after applying  $\mu_0 H = -52$  mT such that  $\mathbf{H}$  had pointed in  $-x$ -direction. The bright (dark) regions in **(h)** represent Py (Si substrate).

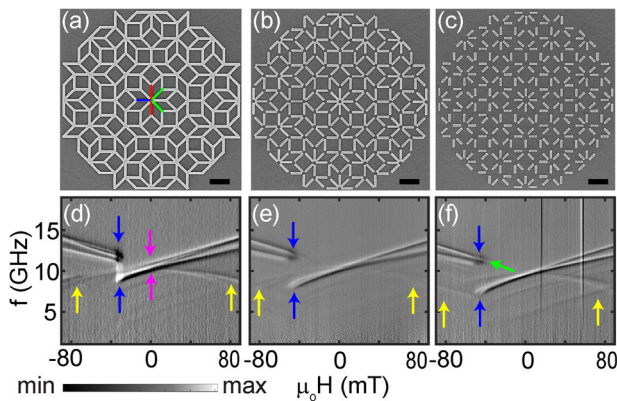
From sample P3A to P3C the lengths of nanobars reduce and the demagnetization effect enhances, thereby reducing the internal fields and consequently the resonance frequencies<sup>33</sup>. Below the prominent branches manifolds of further resonances are found which are attributed partly to standing spin waves confined along the nanobars. Due to the corresponding backward volume magnetostatic spin-wave configuration their resonance frequencies reside at small values. We consider the field regime between the blue arrows in Fig. 1e to be the regime in which nanobars of sample P3A reverse. The switching field regime extends from about –30 mT to –65 mT, very similar to a nominally identical interconnected AMQ investigated in ref. 32. Before we report imaging of magnetic configurations in the reversal regime it is instructive to discuss further details of the spin dynamics in the different quasicrystals.

In Fig. 1e, f, the magenta arrows highlight the branches of Type I and Type II nanobars at zero field. In Fig. 1e, the two branches of P3A are clearly split at  $H = 0$ . This is not the case in P3B. Here the two branches are degenerate at  $H = 0$ , indicating that Type I and Type II experience the same internal magnetic field. The

same degeneracy is observed for P3C at  $H = 0$  in Fig. 1g. We attribute the frequency difference observed in Fig. 1e to the coupling between spin-wave modes in Type I and Type II nanobars leading to an avoided crossing. Nanobars in the interconnected AMQ P3A hence interact. The yellow arrow in Fig. 1g highlights a faint branch which exhibits an agility  $df/dH > 0$  for  $H < 0$  and, at  $H = 0$ , approaches the degenerate frequencies of Type I and Type II nanobars. The characteristics of this branch are consistent with the field-dependent resonance frequency of Type III nanobars which are at  $\pm 72^\circ$ . For them,  $H$  is applied almost along their hard-axis direction. A similar faint branch is seen for P3B in Fig. 1f. In P3C we resolve a specific high-frequency mode in the reversal regime (green arrow) which is not observed in P3A and P3B and will be discussed after the presentation of the magnetic imaging.

In Fig. 2d–f, we display spectra of interconnected (ATA), partially connected (ATB) and disconnected nanobars (ATC). For the Ammann tilings, nanobars of Type I, II and III make angles  $\phi = 0^\circ, \pm 45^\circ$ , and  $\pm 90^\circ$ , respectively. The faint branches highlighted by yellow arrows in Fig. 2d–f are found in all three





**Fig. 2 Broadband spin-wave spectroscopy study of Ammann tiling.**

Scanning electron microscopy (SEM) images showing 1st generation Ammann tilings (AT) (a) ATA for which nanobars are fully connected, (b) ATB with partially connected nanobars and (c) ATC with disconnected nanobars. The Type I, Type II, and Type III nanobars are indicated by blue, green and red colored lines, respectively, in (a). The black color scale bar represents 1 micrometer. Gray-scale spin-wave spectra obtained on 4th generation (d) ATA, (e) ATB and (f) ATC. The magnetic field was applied along the horizontal direction of graphs (a)–(c) and varied from +90 mT to –90 mT in a step-wise manner. In a relatively small field regime near the blue arrow in (d)–(f) the reversal of AT takes place. The magenta color arrows mark  $H = 0$ . The yellow arrows in (d)–(f) highlight the branches attributed to nanomagnets being perpendicular to the applied field. The green arrow in (f) marks the high-frequency mode in the reversal regime of ATC.

Ammann tilings ATA, ATB and ATC, respectively. These branches originate from the Type III nanobars which are at an angle of  $90^\circ$  with respect to the applied field  $H$ .  $H$  thus points along their hard axis. Again at large absolute fields, two prominent branches are found which are consistent with Type I (high frequency) and Type II (second highest frequency) nanobars. Only for the interconnected AMQ ATA we observe a frequency splitting between Type I and Type II nanobars (magenta arrows) near  $H = 0$ .

For AMQs ATB and ATC (disconnected nanobars) the frequency degeneracy occurs. The reversal field regime for ATA (blue arrows in Fig. 2d) is found to be narrow compared to P3A (Fig. 1e). The interconnected nanobars reverse close to  $-30$  mT without a significant switching field distribution. The distribution widens for the other (partly) disconnected AMQs. A detailed analysis of spectra of ATC provides again a specific high-frequency mode (green arrow in Fig. 2f) in the reversal regime, similar to P3C. Spin-wave spectra obtained in minor loops and the reconfigurable characteristics of AMQs are discussed after presenting XPEEM experiments by which we image magnetic states in the hysteretic regime.

**Magnetic imaging of partly reversed quasicrystals.** In the following we discuss magnetic imaging (Fig. 1h) of partly reversed AMQs. We have studied the three designs of AMQs introduced previously<sup>32</sup>, i.e., Penrose P2 and P3 lattices as well as Ammann tilings. In the XPEEM microscope the maximum field  $\mu_0|H_{\max}|$  that was available to magnetize the samples in initial configurations (Fig. 1i of P2A and Supplementary Fig. 3) amounted to 52 mT. This value was smaller than the calculated fields  $\mu_0H_{\text{ani}}$  but larger than the fields that initiated reversal for Type I and Type II nanobars in the broadband spectroscopy experiments of Figs. 1 and 2. Still the field was not large enough to reverse the magnetization of an individual Type III nanobar ( $\phi = \pm 72^\circ$

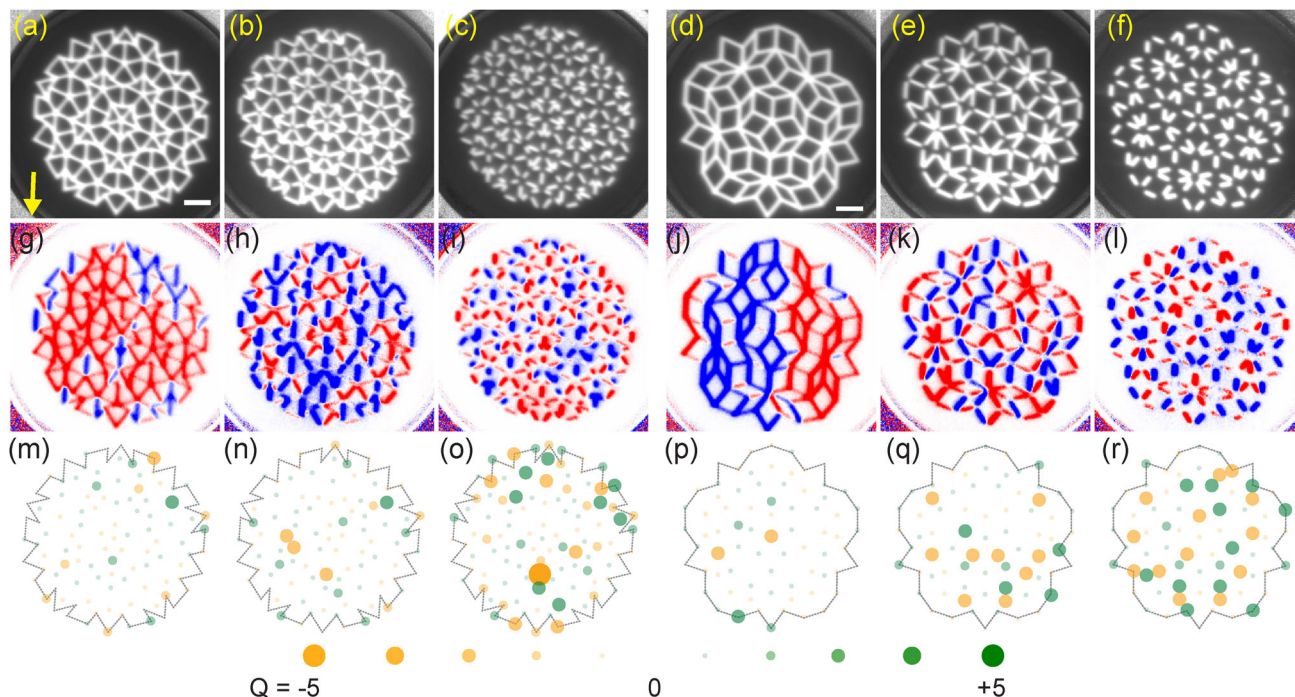
(Penrose) or  $90^\circ$  (Ammann)) if it did not interact with nanobars of Type I and II.

In order to evaluate magnetic states in the saturated and partly reversed quasicrystals, we considered the shape-anisotropy induced bistability (Ising nature) of nanobars and exploited the so-called charge model (CM) (see “Methods”). We first present experimental data obtained on the Penrose lattices (Fig. 3a–f). In Fig. 3g–l, we show XPEEM images (with respective CM analysis shown in Fig. 3m–r) taken on magnetic states of P2 and P3 AMQs after initiating partial reversal in a minor loop (as described in “Methods”). Each image displays a remnant state in zero field after application of a specific field. Images of P2A in Fig. 3g and P3A in Fig. 3j show that these AMQs with interconnected nanobars contain domains or chains of reversed nanobars (blue) next to domains in which nanobars remained in the original orientation (red). In particular P3A incorporates a large-area domain of reversed nanobars. The reversed domains and chains are found to include reversed nanobars of Type III though their anisotropy field was estimated to be larger than the applied reversal field. The detection of reversed Type III nanobars reflects a cooperative phenomenon in the magnetic hysteresis of a quasicrystal. Their reversal is not triggered by the relatively weak external field alone. The reversal is attributed to the influence of neighboring Type I and Type II nanobars which exhibit  $|\phi| \leq 36^\circ$ . The analysis in terms of the CM (see Supplementary Fig. 4) displayed in Fig. 3m, p shows that vertices formed by the interconnected nanobars exhibit overall small values of  $Q$  in their remnant states (the maximum value amounts to  $Q = 3$  in Fig. 3m, p).

AMQs from partially and fully separated nanobars, imaged as P2B (Fig. 3h), P2C (Fig. 3i), P3B (Fig. 3k), and P3C (Fig. 3l), show numerous reversed magnets that are distributed over the whole AMQ compared to the two AMQs with completely interconnected nanobars. The entropy parameter<sup>34</sup> calculated from analyzed XPEEM images shows that the maximum in entropy coincides with the maximum in flux closure loops (Supplementary Fig. 6). From XPEEM images, we found that switching events in the form of major avalanches were seen in the interconnected (exchange-coupled) P2A and P3A samples but were not seen in the disconnected P2C and P3C samples (Supplementary Fig. 7). In the latter samples, opposing nanobars formed fragmented domains which might not be functional for the proposed magnon steering.

In Fig. 4, we analyze the reversal in the AMQs in detail. In Fig. 4a–f, the relative numbers of reversed nanobars are depicted as extracted from a series of XPEEM microscopy images taken at remanence after applying different magnetic fields  $H$ . For P2A and P2B we find reversals to start from Type I nanobars (red symbols in Fig. 4a). For the other AMQs P2C, P3A, and P3B, Type II nanobars switch first. Once Type I or Type II nanobars reverse in the interconnected P2A or P3A, the reversal of their Type III nanobars follows. A less pronounced successive reversal of Type III nanobars is found for P2B and P3B. Here, the number of reversed Type III nanobars is much smaller compared to P2A and P3A. In P2C and P3C consisting of completely disconnected nanobars we do not find the reversal of Type III nanobars in the accessible field regime. Here, the interaction between nanomagnets is too small.

In Fig. 4g–l, we show the total charge  $Q_{\text{tot}}$  extracted from XPEEM images. In AMQs P2A, P2B and P2C the onset of reversal is accompanied by a small global minimum in  $Q_{\text{tot}}$ . In case of P2A and P2B  $Q_{\text{tot}}$  regains a value close to the initial state at large  $H$ . This is different for P2C for which  $Q_{\text{tot}}$  grows with increasing reversal field. For the Penrose P3 tiling consisting of interconnected nanobars (P3A),  $Q_{\text{tot}}$  stays small at large  $\mu_0H$  (vertex charges analyzed for +52 mT are displayed in Supplementary Fig. 4). A growth of  $Q_{\text{tot}}$  is observed for P3B and P3C.



**Fig. 3 Magnetization reversal study of Penrose P2 and P3 artificial magnetic quasicrystals (AMQs) via X-ray photoemission electron microscopy (XPEEM).** **a–f** XPEEM topography images for six different quasicrystals as labeled in the graphs. Bright (dark) regions correspond to magnetic (non-magnetic) material. The scale bar given in **(a)** corresponds to 1  $\mu\text{m}$ . The arrow in **(a)** represents the X-ray direction and the magnetic field direction. Selected magnetic images of remnant states using XPEEM after applying different field values  $\mu_0 H$  (given in parenthesis) for **(g)** P2A (32.5 mT), **(h)** P2B (41.6 mT), **(i)** P2C (42.64 mT), **(j)** P3A (36.4 mT), **(k)** P3B (42.9 mT), and **(l)** P3C (48.1 mT) representing the switching of 44%, 51%, 46%, 56%, 44%, and 55% type I nanobars, respectively. Blue (red) colors represent magnetization parallel (opposite) to the X-ray direction. Blue color indicates a reversed nanobar. The images represent the states attained when about 50% of Type I nanobars switched. Notice the weak contrast in case of nanobars which do not point along the X-ray direction. **m–r** Charge model (CM) analysis of the X-ray magnetic circular dichroism (XMCD) experimental data shown in **(g)–(l)**. The green and orange filled circles at the vertices represent positive and negative vertex charges, respectively. Here the circles with smallest and largest diameter and intensity represent charge  $|Q| = 0$  and  $|Q| = 5$ , respectively. When quasicrystals consist of disconnected nanobars a large charge of up to  $|Q| = 5$  can be found. The magnetic configurations of P2 and P3 tilings in the as-grown state are displayed in Supplementary Fig. 1.

We attribute the growth in  $Q_{tot}$  to the fact that disconnected nanobars of Type III do not experience cooperative reversal.

In Fig. 4m–r, we summarize the number of flux-closure loops (FCLs) present in the XPEEM images. For Penrose P2 tilings the minimum in  $Q_{tot}$  is accompanied by a maximum of FCLs. The maximum in FCLs roughly occurs when about 50% of Type I and Type II nanobars have undergone switching. For P3B a pronounced maximum in FCLs is found as well. For P3C the corresponding variation is small. Note that P2B, P2C and P3B exhibit a large number of FCLs already before pronounced switching has taken place. We attribute this observation to the limited field strength (52 mT) that was available to define the initial magnetic states (Supplementary Fig. 3). The maximum field was not large enough to saturate Type III nanobars that were not connected to neighboring nanobars.

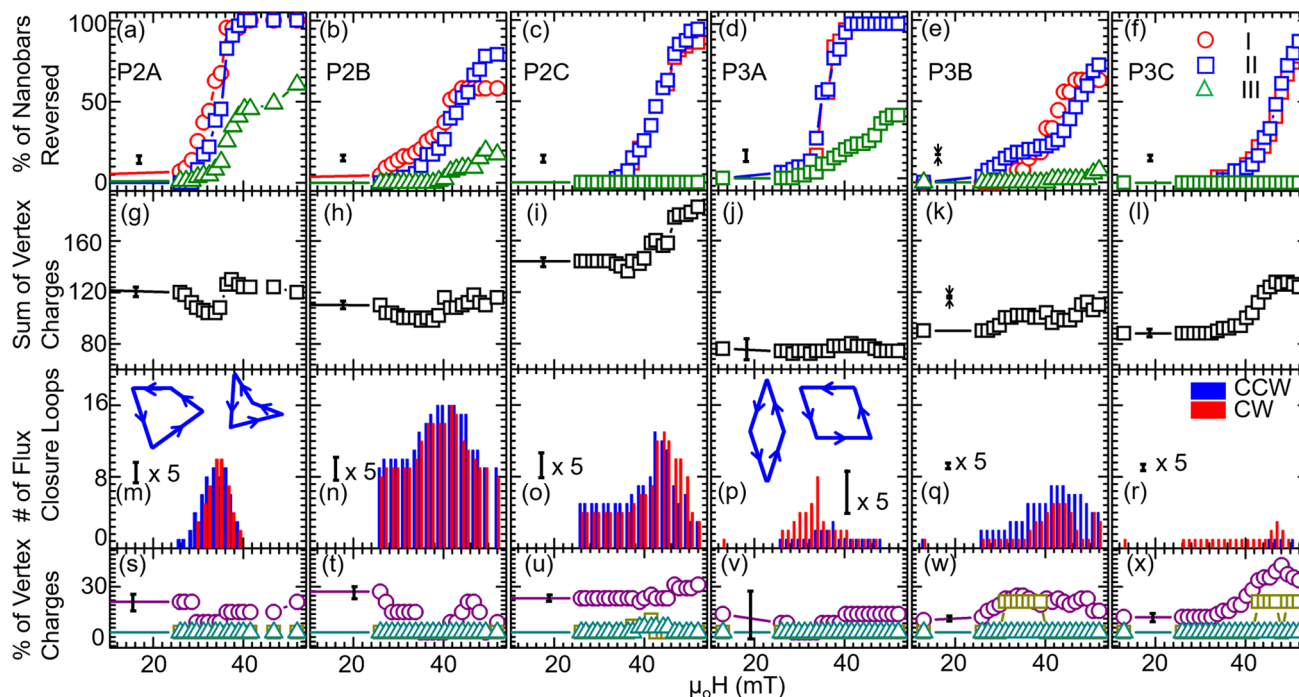
In Fig. 4s–x, we depict the number of individual vertices that exhibit the maximum charge  $Q = 3$ ,  $Q = 4$  and  $Q = 5$  for neighbor numbers  $N = 3$ ,  $N = 4$  and  $N = 5$ , respectively. For interconnected lattices P2A and P2B the number of vertices with  $Q = 4$  and  $Q = 5$  is negligible. The number of vertices with  $Q = 3$  takes its lowest value when the maximum number of FCLs is reached in P2A. A similar behavior is observed for P2B and P3A. P2C, P3B, and P3C behave differently in that the number of vertices with  $Q = 3$  does not go through a global minimum as a function of reversal field. In case of P2C and P3C the number grows with  $H$ . A considerable number of vertices with  $Q = 4$  ( $Q = 5$ ) is found only in P3B and P3C (P2C). Large individual vertex charges hence occur in Penrose P2 and P3 tilings with

disconnected nanobars, but not for P2 and P3 tilings with interconnected ones. In the latter cases, vertex configurations with large  $Q$  (as stabilized in micromagnetic simulations for interconnected nanobars in Fig. 5a) have thus not been observed in the reversal regime. The real AMQ lattices made from interconnected nanobars avoided these high-energy configurations and formed FCLs instead. We argue that the exchange interaction in the vertices of the interconnected P2 and P3 tilings plays the major role for the observed cooperative magnetization reversal which included Type III nanobars.

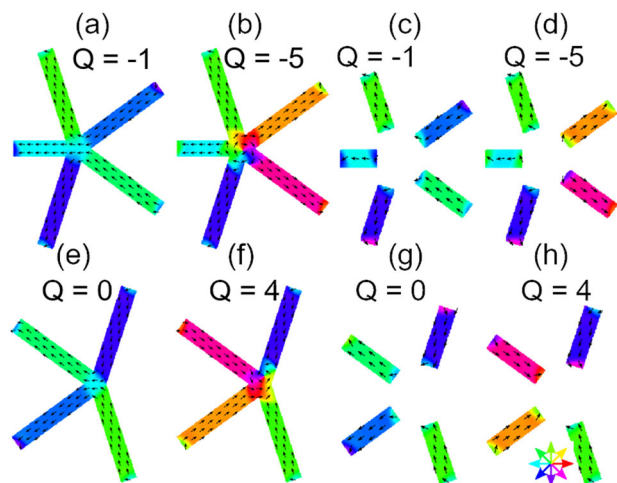
Precursors for the cooperative reversal are the Type I and Type II nanobars that meet at a vertex exhibiting a relatively large charge (e.g.,  $Q = 2$  for  $N = 4$ ). The occurrence of large  $Q$  indicates the violation of the local ice rule. Figure 4s–x reveals that ice rule violations are pronounced in P2C, P3B and P3C with disconnected nanobars. Our data suggest that weakly interacting nanobars in AMQs provoke ice rule violations. Note that P3B and P3C did not show the frequency splitting between Type I and Type II nanobar resonances near  $H = 0$  (Fig. 1f, g). The absence of splitting is consistent with weakly interacting nanobars.

To gain further insight into the violation of spin ice rules we have simulated low- and high-energy vertex states for connected and disconnected nanobars (Fig. 5). We see that for interconnected nanobars found e.g., in P2A, the total vertex energy increases by about 80% from Fig. 5a ( $Q = -1$ ) to Fig. 5b ( $Q = -5$ ), respectively, considering a vertex with  $N = 5$ . For the disconnected nanobars relevant e.g., in P2C, a violation of the spin ice rule ( $Q = -5$  in Fig. 5d) causes an energy higher by only





**Fig. 4 Magnetization reversal analysis of Penrose P2 and P3 artificial magnetic quasicrystals (AMQs).** **a-f** Field-dependent reversal of Type I (red circle), Type II (blue square) and Type III (green triangle) in AMQs P2A, P2B, P2C, P3A, P3B, and P3C, respectively. **g-l** Total charge  $Q_{\text{tot}}$  for P2A, P2B, P2C, P3A, P3B, and P3C, respectively. **m-r** Number of clockwise (CW) and counter-clockwise (CCW) flux-closure loops (FCLs) (see the insets in **(m)** and **(p)** for their definition) for P2A, P2B, P2C, P3A, P3B, and P3C, respectively. **s-x** Evaluation of relative amounts of maximum possible individual vertex charges  $Q$  in P2A, P2B, P2C, P3A, P3B, and P3C, respectively. The purple, dark yellow, and dark cyan colored symbols represent charges 3 (for  $N=3$ ), 4 (for  $N=4$ ), and 5 (for  $N=5$ ), respectively. The values in **(s)**, **(t)** and **(v)** were multiplied by 3 for better visualization using a unique y scale for all graphs. Notice the presence of charges  $|Q|=5$  in P2C for  $N=5$  vertices. The error bars are calculated based on the number of nano bars below the noise level of the background (that is, the signal-to-noise ratio is below 1). The error bars in **(m)**–**(r)** are multiplied by five times for better comparison purposes.



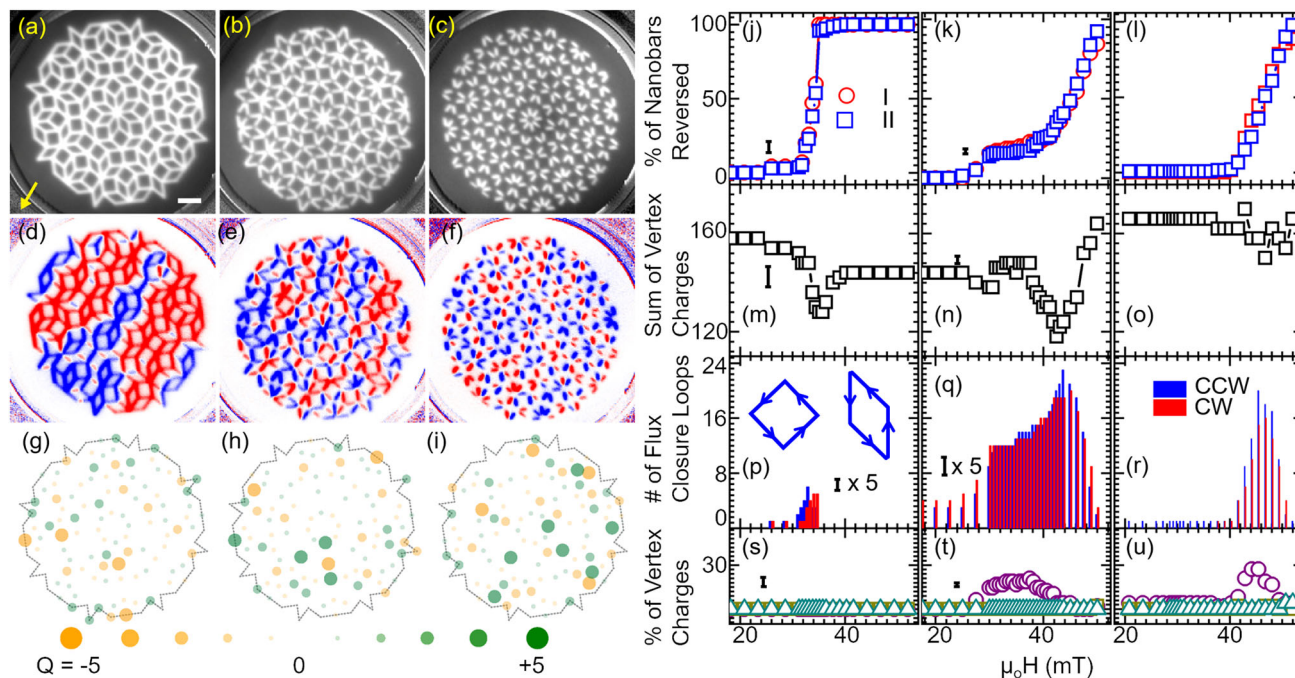
**Fig. 5 Total energy determination for different arrangement of nanobars via micromagnetic simulations.** Simulated magnetization directions (black arrows and color wheel) for representative connected and disconnected bars on Penrose **(a)–(d)** P2 and **(e)–(h)** P3 tilings. The total energies in units of  $10^{-16}$  J are **(a)** 1.01, **(b)** 1.85, **(c)** 1.20, **(d)** 1.30, **(e)** 0.83, **(f)** 1.51, **(g)** 0.96, and **(h)** 1.03, respectively. The values  $Q$  depicted in the graphs indicate the total charge of the respective input magnetization configuration.

7% compared to Fig. 5c ( $Q = -1$ ). Consistent energy variations with  $Q$  are found for vertices with  $N=4$  in Fig. 5e–h. The large energy cost for a spin ice rule violation found in simulations for fully interconnected nanobars favors low vertex charges which agree with the spin ice rule. Simulated magnetization reversal of

different AMQs shows that interconnected nanobars undergo reversal in a narrow magnetic field range as opposed to nanobars that are coupled via weak dipolar interaction (Supplementary Fig. 8).

The simulations show the absence of charges  $Q$  of magnitude  $\pm 5$  in the interconnected samples whereas the weakly coupled arrays, P2C, P3C and ATC, show the presence of  $Q = \pm 5$ . Indeed we experimentally detected mainly low- $Q$  states in the interconnected lattices of P2A, P3A and ATA in the reversal regime. If present, high- $Q$  (high energy) vertices in interconnected AMQs act as nucleation sites for the cooperative reversal. They give rise to non-stochastic switching<sup>23</sup>, presumably causing the staircase-like jumps or knee anomalies<sup>3</sup>. Vertices containing disconnected nanobars are found to accommodate particularly large  $Q$  and violate the spin ice rule. However these charges do not trigger cooperative reversal which we attribute to the relatively weak dipolar coupling in our AMQs. Still our results indicate that dipolar interaction is enough to provoke energy minimization on a local scale between vertices via flux-closure loops. We find an increase in the number of flux-closure loops in almost any of the investigated quasicrystals in the reversal regime. The dipolar interaction and loop formation are however not sufficient for creating extended domains.

In Fig. 6 we summarize the experimental data obtained on Amman tilings (AT) depicted in Fig. 6a–c. The initial magnetic configurations are displayed in Supplementary Fig. 5. The XPEEM experiments are shown in Fig. 6d–f. For interconnected nanobars we detect a large central domain of reversed nanobars. For the partially and fully disconnected nanobars the reversed nanobars are more distributed over the AMQs. In analogy to disconnected Penrose tilings the analysis based on the CM



**Fig. 6 The magnetization reversal study of Ammann artificial magnetic quasicrystals (AMQs) using X-ray photoemission electron microscopy (XPEEM).** XPEEM topography image for Ammann tilings (a) ATA ( $\mu_0 H = 34$  mT), (b) ATB (at 47 mT), and (c) ATC (at 47 mT) representing the switching of 47%, 47%, and 53% Type I nanobars. Bright (dark) regions correspond to magnetic (non-magnetic) regions. The scale bar corresponds to  $1 \mu\text{m}$ . The arrow represents the field direction. The X-ray direction was misaligned by  $22^\circ$  to optimize the detection of nanobars of all the different orientations. **d-f** X-ray magnetic circular dichroism (XMCD) data of topography images shown in (a)–(c). Blue (red) colors represent magnetization parallel (opposite) to the X-ray direction. Blue color indicates a reversed nanobar. Notice the weak contrast of nanobars whose orientation deviates from the X-ray direction. The magnetic configurations of Ammann tilings in the as-grown state are displayed in Supplementary Fig. 2. **g-i** Charge model (CM) analysis of XMCD experimental data shown in (d)–(f). The green and orange filled circles at the vertices represent positive and negative vertex charges, respectively. Here the circles with smallest and largest diameter and intensity represent charge  $|Q| = 0$  and  $|Q| = 5$ , respectively. **j-l** Classification of reversal in terms of switching of Type I and II of nanobars for ATA, ATB, and ATC, respectively. Legends I and II represent nanobars of Types I and II. **m-o** Total charge count for ATA, ATB, and ATC, respectively. **p-r** Number of clockwise (CW) and counter-clockwise (CCW) flux-closure loops (FCLs) (see the inset in (p) for their definition) for ATA, ATB, and ATC, respectively. **s-u** Charge depiction for ATA, ATB, and ATC, respectively. The purple, dark yellow, and dark cyan colored symbols represent charges 3 ( $N = 3$ ), 4 ( $N = 4$ ), and 5 ( $N = 5$ ), respectively. The error bars are calculated based on the number of nano bars below the noise level of the background (that is, the signal-to-noise ratio is below 1). The error bars in Fig. 5p, q are multiplied by five times for better comparison purposes.

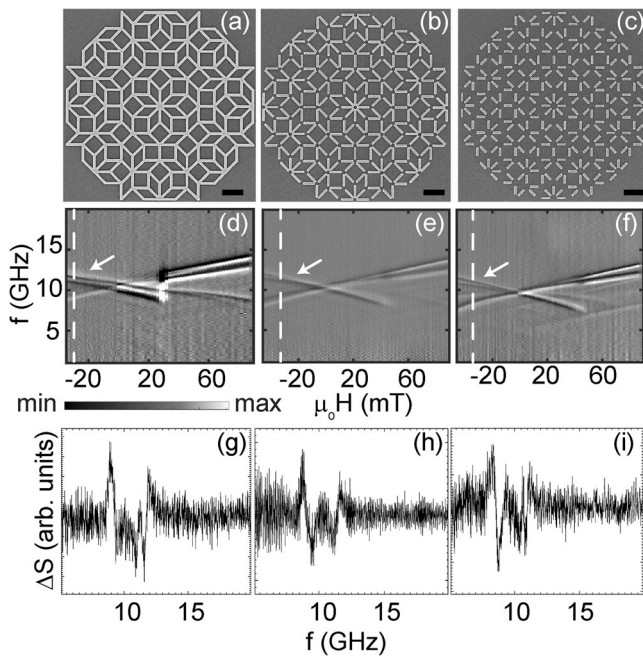
provides a tendency toward slightly larger individual vertex charges when going from ATA to ATC. Still this tendency is less significant in the graphs of Fig. 6g–i compared to the Penrose tilings. Analyzing all our XPEEM datasets we find that almost all of Type III nanobars with  $\phi = \pm 90^\circ$  do not undergo switching in Ammann tilings (compare also data taken at  $+52$  mT and shown in Supplementary Fig. 5). Studying the reversal of Type I and Type II nanobars in detail (Fig. 6j–l) ATA shows a narrower switching field distribution for these nanobars compared to P2A and P3A. About 40% of Type I and Type II nanobars of ATA undergo reversal within a span of 7.5 mT (Fig. 6j), i.e., within a field regime smaller than for P2A and P3A. Full reversal of the Type I and Type II nanobars is seen at about 34 mT. The corresponding nanobars that are disconnected require a field of up to about 52 mT for full reversal. These observations are qualitatively consistent with the field dependencies of spin-wave resonances presented in Fig. 2. We suppose that the narrow field distribution for switching in ATA reflects a cooperative reversal phenomenon like an avalanche (compare the blue chain-like domain in Fig. 6d).

The analysis of total charges  $Q_{tot}$  is depicted in Fig. 6m–o. In all three Ammann tilings we observe a minimum in  $Q_{tot}$  when Type I and Type II nanobars undergo the reversal process. The drop in  $Q_{tot}$  is accompanied by an increased number of FCLs (Fig. 6p–r). In the magnetization reversal of ATB (Fig. 6k) the switching

seems to take place in two separate steps (see the increases in the number of reversed nanobars at 28 mT and 42 mT in Fig. 6k). Consistent with these features, there are local minima (a shoulder and a maximum) in  $Q_{tot}$  (FCLs). We also see that the maximum in FCLs coincides with the minimum in the sum of charges. The slope of reversal in ATC (Fig. 6l) resembles the high-field slope of ATB in Fig. 6k and the ones seen in P2B, P2C and P3C. We argue that the high-field reversal processes which are detected over a broad field regime reflect the disconnected nanobars. In this field regime we find the spin ice rule violations for ATB and ATC (Fig. 6t, u, respectively) in that the maximum vertex charge  $Q = 3$  is present in case of  $N = 3$ . This large vertex charge is not observed in the reversal of ATA (Fig. 6s).

The data shown in Fig. 4d are consistent with the evolution of spin-wave branches. Reversal of P3A starts near 30 mT via switching of Type I and Type II nanobars. The switching of Type III nanobars occurs at higher fields. At 52 mT, i.e., the maximum field in the XPEEM microscope, less than 50% have been switched. Consistently, in our spectroscopy data we need to apply an opposing field with  $\mu_0 |H| = 70$  mT to obtain fully developed high-frequency spin-wave branches in Fig. 1e. In P3B (Fig. 4e) and P3C (Fig. 4f) we do not find reversed Type III nanobars up to 52 mT in XPEEM, which explains the faint monotonous spin-wave signals marked by a yellow arrow in Fig. 1g. The evolution of spin-wave branches measured on ATA (Fig. 2d) is also





**Fig. 7 Broadband spin-wave spectroscopy spectra under the application of minor loop field protocol in Ammann tilings (ATs).** Scanning electron microscopy (SEM) images showing 1st generation Ammann tilings **(a)** ATA for which nanobars are fully connected, **(b)** ATB with partially connected nanobars and **(c)** ATC with disconnected nanobars. The black color scale bar represents 1 micrometer. Gray-scale spin-wave spectra for large arrays measured on 4th generation **(d)** ATA, **(e)** ATB, and **(f)** ATC, respectively. The minor loop magnetic field protocol implemented was **(d)**  $+90\text{ mT} \rightarrow -34\text{ mT} \rightarrow 90\text{ mT}$ , **(e)**  $+90\text{ mT} \rightarrow -46\text{ mT} \rightarrow 90\text{ mT}$ , and **(f)**  $+90\text{ mT} \rightarrow -46\text{ mT} \rightarrow 90\text{ mT}$ , respectively. The line spectra  $\Delta S$  for **(g)** ATA, **(h)** ATB and **(i)** ATC at  $-30\text{ mT}$  (extracted at the white dashed lines in **(d)**–**(f)**, respectively).

consistent with the XPEEM imaging (Fig. 6j): a large number of Type I and Type II nanobars reverse in a narrow regime between 30 and 34 mT in both experiments. Type III nanobars do not reverse in Fig. 6j explaining the monotonous variation of the branch highlighted by yellow arrows in Fig. 2d.

**Broadband spin-wave spectroscopy in the minor loop: reconfigurable magnon excitations.** In the following we discuss the magnonic excitations which are detected in minor loop measurements starting from intermediate negative fields after magnetizing ATA, ATB and ATC at  $+90\text{ mT}$ . In Fig. 7 we show color-coded spin-wave spectra taken on partially reversed quasicrystals. In each case the depicted spectra belong to a minor loop which starts near the magnetic field value for which the XPEEM data suggest a minimum in the sum of vertex charges and a large number of flux-closure loops for the Ammann tilings. XPEEM images for ATA (Fig. 7a), ATB (Fig. 7b), and ATC (Fig. 7c) were shown in Fig. 6d–f, respectively. For these three samples the branches in the minor loop (Fig. 7d–f) are more complex compared to major loop measurements. They exhibit both  $df/dH > 0$  and  $df/dH < 0$  for  $H < 0$  reflecting non-reversed and reversed nanobars, respectively. The white arrows highlight branches which were not observed in Fig. 2d–f. The number of flux-closure loops does not seem to be large enough to resolve additional x-shaped magnon branches near  $H = 0$  which are characteristic for spin dynamics in magnetic vortex configurations<sup>35,36</sup>.

The linewidths of the individual spin-wave branches indicated by white arrows in Fig. 7d–f amount to 0.33, 0.54 and 0.29 GHz,

respectively, at  $-30\text{ mT}$ . We have extracted the linewidths from the line spectra  $\Delta S$  shown in Fig. 7g–i by measuring the frequency difference  $\delta f$  between the local minimum and maximum of each of the right-most resonances. All the reprogrammed branches in Fig. 7 obtained in the minor loop measurements exhibit small linewidths which are similar to the linewidths observed in the major loops. Quasicrystalline tilings studied here can accommodate a larger number of nanobars in a given area than periodic tilings. This feature of AMQs enhances their device functionality in terms of absorption strength (that is based on the number of spins, i.e., nanobars). The Ammann and Penrose tilings possess higher rotational symmetries compared to periodic tilings, thus giving an enhanced magnonics functionality also in view of the grating coupler effect<sup>37</sup>. The appearance of additional spin-wave branches under the application of the minor loop field protocol enables reconfigurable frequency filters that can be designed out of a quasicrystalline array of nanobars by controlling the size, shape and lattice geometry of the AMQ.

## Conclusions

To conclude, we varied the exchange and dipolar interactions in Penrose P2, P3, and Ammann quasicrystal lattices. We explored magnonic excitations and imaged ferromagnetic reversal in these exotic ASI structures using XPEEM. Our data show compliance with ice rules in the exchange-coupled nanobars. Ice rule violation occurs prominently in tilings without exchange coupling among nanobars. Owing to the asymmetric and aperiodic arrangements around each vertex, nanobars taking the same angle with the applied field have significantly different switching behavior depending on their local environment. We observe the narrowest distribution of reversal fields in an exchange-coupled Ammann tiling, followed by the exchange-coupled Penrose P2 and P3 tilings. Here reversal is triggered by vertices whose charge  $Q$  deviates from the ground state. We demonstrated that spin-wave resonances remain sharp for the partially reversed quasicrystals. The exchange-coupled Penrose P3 and Ammann tilings show the formation of extended domains via non-stochastic cooperative reversal which might be functionalized for reprogrammable magnon steering.

## Methods

**Sample fabrication.** A bilayer PMMA/MMA resist was spin-coated on a silicon substrate, and exposed via Raith electron beam lithography system at 100 keV. After development of the resist a 25 nm thick Py film was deposited using ebeam evaporator. Subsequently, ultrasonic assisted lift-off was performed in N-methyl Pyrrolidone solution.

**XPEEM measurements.** X-ray photoemission electron microscopy (XPEEM) imaging was done at the SPEEM station located at the UE49/PGMa beamline at BESSY-II (Helmholtz Zentrum, Berlin). The samples were mounted on a sample holder which allowed us to apply magnetic field to the sample in-situ. The Penrose P2 and P3 AMQs were patterned on the same silicon substrate, whereas Ammann AMQs were fabricated on another identical silicon substrate. The Magnetic images were obtained by performing XMCD at the Fe L3-edge. The obtained contrast is a measure of the projection of the magnetization on the X-ray polarization vector. Thus nanobars with a magnetization parallel or antiparallel to the X-ray polarization either appear red or blue. The sample orientation was optimized to maximize the contrast.

**Broadband spin-wave spectroscopy.** To detect the resonances, we connected two ports of a vector network analyzer to both ends of the CPW using microwave probes and coaxial cables. Subsequently, we applied a constant global magnetic field (from  $\pm 90\text{ mT}$  to  $\mp 90\text{ mT}$  in steps of  $\pm 1\text{ mT}$ ) at a given in-plane angle  $\phi$  and performed frequency sweeps from 1 GHz up to 20 GHz using a vector network analyzer. We collect the S-parameters from the vector network analyzer as a function of frequency at the constant applied magnetic field,  $\mu_0 H$ , and angle  $\phi$ , and this corresponds to single spin-wave spectra at one  $\mu_0 H$  and  $\phi$  value. We then subtracted spin-wave spectra taken at successive fields  $\mu_0 H_i$ ; that is, we obtain  $\Delta S(i) = S[H(i+1), \phi] - S[H(i), \phi]$  ( $i = 1, 2, 3, \dots$ ).



**Micromagnetic simulations.** Simulations were performed using the Object Oriented MicroMagnetic Framework (OOMMF) code<sup>38</sup>, and the Py parameters used in simulations were as follows: Exchange constant  $A = 1.3 \times 10^{-11} \text{ J m}^{-1}$ , saturation magnetization  $M_S = 8 \times 10^5 \text{ A m}^{-1}$ , magnetocrystalline anisotropy constant  $K = 0$ , gyromagnetic ratio  $\gamma = 2.211 \times 10^5 \text{ m A}^{-1} \text{ s}^{-1}$ , and dimensionless damping coefficient  $\alpha = 0.01$ . Different magnetic configurations were explored by initializing magnetization vectors of individual segments and relaxing the spin system at the given magnetic field. For this, we first created a colored bitmap (on a grid of  $5 \text{ nm} \times 5 \text{ nm} \times 25 \text{ nm}$ ) where each segment was assigned a color corresponding to its assumed magnetization orientation. We then imported this colored bitmap into OOMMF and equilibrated it in the presence of a field that resided within the experimental switching regime. For the magnetization reversal simulations, we used  $10 \text{ nm} \times 10 \text{ nm} \times 25 \text{ nm}$  grid to keep the total computational time manageable.

**Charge model.** The charge model (CM) assigns a magnetic charge to each of the vertices for evaluating the magnetic energy<sup>7</sup>. For this one assumes each nanobar to be a dumbbell of length  $l$  with two equal charges of opposite polarity,  $\pm q = \pm m/l = \pm Mt/wl = \pm Mt/w$ , at the dumbbell's ends.  $m$ ,  $M$ ,  $t$ , and  $w$  represent the magnetic dipole moment, saturation magnetization, thickness, and width of a segment, respectively. A vertex with a coordination number (CN)  $N$  can acquire a charge  $Q = \sum q = +Nq \dots -Nq$  which is the sum of individual charges  $q$ . For a given CN a vertex acquires the lowest possible charge  $Q$  in the ground state to minimize the total energy. In the text we provide value of  $Q$  in units of  $q$ .

### Data availability

Requests concerning data should be addressed to V.S.B. or D.G. The datasets analyzed in the current study are available in the Zenodo repository, <https://doi.org/10.5281/zenodo.8109424>.

### Code availability

The code used for micromagnetic simulations is found in ref. <sup>38</sup>.

Received: 16 September 2022; Accepted: 19 July 2023;

Published online: 29 July 2023

### References

- Shechtman, D., Blech, I., Gratias, D. & Cahn, J. W. Metallic phase with long-range orientational order and no translational symmetry. *Phys. Rev. Lett.* **53**, 1951 (1984).
- Goldman, A. I. et al. A family of binary magnetic icosahedral quasicrystals based on rare earths and cadmium. *Nat. Mater.* **12**, 714–718 (2013).
- Bhat, V. S. et al. Controlled magnetic reversal in permalloy films patterned into artificial quasicrystals. *Phys. Rev. Lett.* **111**, 077201 (2013).
- Wang, R. et al. Artificial 'spin ice' in a geometrically frustrated lattice of nanoscale ferromagnetic islands. *Nature* **439**, 303 (2006).
- Qi, Y., Brintlinger, T. & Cummings, J. Direct observation of the ice rule in an artificial kagome spin ice. *Phys. Rev. B* **77**, 094418 (2008).
- Mengotti, E. et al. Real-space observation of emergent magnetic monopoles and associated dirac strings in artificial kagome spin ice. *Nat. Phys.* **7**, 68–74 (2011).
- Castelnovo, C., Moessner, R. & Sondhi, S. L. Magnetic monopoles in spin ice. *Nature* **451**, 42–45 (2008).
- Branford, W., Ladak, S., Read, D., Zeissler, K. & Cohen, L. Emerging chirality in artificial spin ice. *Science* **335**, 1597–1600 (2012).
- Keswani, N. & Das, P. On the micromagnetic behavior of dipolar-coupled nanomagnets in defective square artificial spin ice systems. *J. Appl. Phys.* **126**, 214304 (2019).
- Skjærø, S. H., Marrows, C. H., Stamps, R. L. & Heyderman, L. J. Advances in artificial spin ice. *Nat. Rev. Phys.* **2**, 13–28 (2020).
- Gilbert, I. et al. Direct visualization of memory effects in artificial spin ice. *Phys. Rev. B* **92**, 104417 (2015).
- Arroo, D. M., Gartside, J. C. & Branford, W. R. Sculpting the spin-wave response of artificial spin ice via microstate selection. *Phys. Rev. B* **100**, 214425 (2019).
- Gliga, S., Kákay, A., Hertel, R. & Heinonen, O. G. Spectral analysis of topological defects in an artificial spin-ice lattice. *Phys. Rev. Lett.* **110**, 117205 (2013).
- Iacocca, E., Gliga, S., Stamps, R. L. & Heinonen, O. Reconfigurable wave band structure of an artificial square ice. *Phys. Rev. B* **93**, 134420 (2016).
- Jungfleisch, M. et al. Dynamic response of an artificial square spin ice. *Phys. Rev. B* **93**, 100401 (2016).
- Li, Y. et al. Thickness dependence of spin wave excitations in an artificial square spin ice-like geometry. *J. Appl. Phys.* **121**, 103903 (2017).
- Lendinez, S. & Jungfleisch, M. B. Magnetization dynamics in artificial spin ice. *J. Phys.: Condens. Matter* **32**, 013001 (2019).
- Dion, T. et al. Tunable magnetization dynamics in artificial spin ice via shape anisotropy modification. *Phys. Rev. B* **100**, 054433 (2019).
- Iacocca, E., Gliga, S. & Heinonen, O. G. Tailoring spin-wave channels in a reconfigurable artificial spin ice. *Phys. Rev. Appl.* **13**, 044047 (2020).
- Li, Y. et al. Brillouin light scattering study of magnetic-element normal modes in a square artificial spin ice geometry. *J. Phys. D: Appl. Phys.* **50**, 015003 (2016).
- Brajuskovic, V., Barrows, F., Phatak, C. & Petford-Long, A. Real space observation of magnetic excitations and avalanche behavior in artificial quasicrystal lattices. *Sci. Rep.* **6**, 34384 (2016).
- Farmer, B. et al. Direct imaging of coexisting ordered and frustrated sublattices in artificial ferromagnetic quasicrystals. *Phys. Rev. B* **93**, 134428 (2016).
- Bhat, V. et al. Non-stochastic switching and emergence of magnetic vortices in artificial quasicrystal spin ice. *Phys. C: Supercond. Appl.* **503**, 170–174 (2014).
- Shi, D. et al. Frustration and thermalization in an artificial magnetic quasicrystal. *Nat. Phys.* **14**, 309 (2018).
- Wang, Y.-L. et al. Rewritable artificial magnetic charge ice. *Science* **352**, 962 (2016).
- Stamps, R. L. et al. *Spin Waves on Spin Structures: Topology, Localization, and Nonreciprocity* 2nd edn, chap. 8, 219–260 (CRC Press, 2017)
- Penrose, R. Pentaplexity—a class of non-periodic tilings of the plane. *Math. Intell.* **2**, 32 (1979).
- Perković, O. & Sethna, J. P. Improved magnetic information storage using return-point memory. *J. Appl. Phys.* **81**, 1590–1597 (1997).
- Aharoni, A. Demagnetizing factors for rectangular ferromagnetic prisms. *J. Appl. Phys.* **83**, 3432–3434 (1998).
- Coey, J. M. D. *Magnetism and Magnetic Materials* 4th edn (Cambridge University Press, 2014).
- Burn, D., Chadha, M. & Branford, W. Angular-dependent magnetization reversal processes in artificial spin ice. *Phys. Rev. B* **92**, 214425 (2015).
- Bhat, V. S. & Grundler, D. Angle-dependent magnetization dynamics with mirror-symmetric excitations in artificial quasicrystalline nanomagnet lattices. *Phys. Rev. B* **98**, 174408 (2018).
- Gurevich, A. G. & Melkov, G. A. *Magnetization Oscillations and Waves* (CRC Press, 1996).
- Gonzalez, R. C. *Digital Image Processing* (Pearson Education India, 2009).
- Giesen, F. et al. Hysteresis and control of ferromagnetic resonances in rings. *Appl. Phys. Lett.* **86**, 112510 (2005).
- Podbielski, J., Giesen, F. & Grundler, D. Spin-wave interference in microscopic rings. *Phys. Rev. Lett.* **96**, 167207 (2006).
- Yu, H. et al. Omnidirectional spin-wave nanograting coupler. *Nat. Commun.* **4**, 2702 (2013).
- Donahue, M. & Porter, D. Oommf user guide, version 1.0. Interagency Report NISTIR 6376 (1999).

### Acknowledgements

The research was supported by the Swiss National Science Foundation via Grant No. 163016. We thank HZB for the allocation of synchrotron radiation beamtime. V.S.B. acknowledges support from the foundation for Polish Science through the IRA Programme financed by EU within SG OP Programme.

### Author contributions

V.S.B. and D.G. conceived the project. V.S.B. fabricated the samples and performed the micromagnetic simulations. V.S.B., S.W., F.K., and K.B. conducted the XPEEM experiments. V.S.B., S.W., and D.G. performed the data analysis and wrote the manuscript on which all authors commented.

### Competing interests

The authors declare no competing interests.

### Additional information

**Supplementary information** The online version contains supplementary material available at <https://doi.org/10.1038/s42005-023-01310-0>.

**Correspondence** and requests for materials should be addressed to Vinayak Shantaram Bhat or Dirk Grundler.

**Peer review information** *Communications Physics* thanks Vuk Brajuskovic, and the other, anonymous, reviewer(s) for their contribution to the peer review of this work.

**Reprints and permission information** is available at <http://www.nature.com/reprints>

**Publisher's note** Springer Nature remains neutral with regard to jurisdictional claims in published maps and institutional affiliations.



**Open Access** This article is licensed under a Creative Commons Attribution 4.0 International License, which permits use, sharing, adaptation, distribution and reproduction in any medium or format, as long as you give appropriate credit to the original author(s) and the source, provide a link to the Creative Commons licence, and indicate if changes were made. The images or other third party material in this article are included in the article's Creative Commons licence, unless indicated otherwise in a credit line to the material. If material is not included in the article's Creative Commons licence and your intended use is not permitted by statutory regulation or exceeds the permitted use, you will need to obtain permission directly from the copyright holder. To view a copy of this licence, visit <http://creativecommons.org/licenses/by/4.0/>.

© The Author(s) 2023